RSC Advances

PAPER

View Article Online
View Journal | View Issue

Cite this: *RSC Adv.*, 2026, **16**, 2597

Hydrolysis mechanisms for A-series (Novichok) nerve agents at different pH V and computational simulant screening

Junjun Jia,[ab] Wenjie Duan,[b] Qingyuan Li,[ab] Xinxin Xu,[ab] Zhenbang Tian[b] and Zhongliang Zhang *[ba]

Received 8th December 2025
Accepted 2nd January 2026

DOI: 10.1039/d5ra09488g

rsc.li/rsc-advances

A-series nerve agents (Novichok agents) are ultratoxic organophosphorus agents that were listed in Schedule 1 of the Chemical Weapons Convention in 2019. Their extreme acute toxicity precludes direct experimental manipulation, and theoretical investigations into their aqueous degradation mechanisms and safe simulant development are scarce. This study investigated the dominant hydrolysis pathways of three A-series nerve agents (A230, A232, and A234) under various pH conditions, along with their corresponding hydrolysis half-lives, using computational methods. The hydrolysis rates of the nerve agents exhibited a strong pH dependence, with acid- and base-catalyzed hydrolysis resulting in a characteristic bell-shaped curve of half life *versus* pH. Computational screening identified *N*′-diphenoxyphosphorylethanimidamide (ADPP) and 4-nitrophenyl (*E*)-*N*-(1-(diethylamino)ethylidene)-P-methylphosphonamidate as optimal hydrolysis simulants. The experimental hydrolysis results for ADPP strongly agreed with the theoretical predictions, confirming the reliability of the methodology. Overall, this study established a predictive framework to determine the dominant hydrolysis pathways and half-lives of amidinofluorophosphonates, enabling the estimation of hydrolysis properties for potential A-series agents based solely on their molecular formulas.

Introduction

Organophosphorus compounds are used globally as herbicides and insecticides owing to their high biological toxicity.[1] The most toxic representatives are classified as nerve agents, and they have been repeatedly weaponized and used in targeted assassinations and military operations.[2] Organophosphorus nerve agents currently include G-series, V-series, GV-series, and A-series nerve agents (NAs).[3–5] While the physicochemical and toxicological profiles of the "classical" G- and V-agents are well-documented, reliable data on the A-series are fragmented.[6,7] The first credible disclosure of Novichok structures was made by Mirzayanov;[8] however, these agents only gained public awareness after the 2018 Salisbury attack in the United Kingdom.[9,10] Despite these agents being formally added to Schedule 1 of the Chemical Weapons Convention in 2019, they have been used in subsequent assassinations.[11]

The current understanding of NAs is limited.[12] Previous research has primarily focused on structural elucidation, spectroscopic characteristics, and mass spectrometric behaviors.[13–24] Collectively, these studies revealed that Novichok agents are not only more acutely toxic than VX but also more persistent in the environment. For example, A234 retains measurable activity on sandy soils and indoor surfaces for weeks to months, a property that considerably complicates containment and decontamination.[25–29]

Water, as a ubiquitous environmental medium and a recognized green solvent, has been used in studies investigating NA degradation in aqueous phases. The half life of A234 in neutral aqueous solution is approximately 10–30 days,[30,31] and it can exist for a long time under mildly acidic or alkaline conditions.[18,32]

Beyond purely hydrolytic conditions, catalytic strategies to accelerate the degradation of A-series nerve agents have been investigated, including MOF (Metal–Organic Framework) catalysis,[33] enzyme catalysis,[34] skin decontamination lotion catalysis,[26] and acid, alkali, and oxidant catalysis.[28]

The extreme toxicity of Novichok agents prohibits direct experimental handling, underscoring the importance of theoretical computational approaches in this field. Otsuka and Miyaguchi[35] investigated the reaction mechanism between NAs and OH^- using theoretical calculations. Their results indicated that the dissociation energy barrier for F^- was significantly lower than that for NR^- in alkaline environments. Imrit *et al.*[36] analyzed the hydrolysis pathways of A234 using density functional theory (DFT) and reported that hydrolysis at the

[a]*School of Material Science and Engineering, Zhengzhou University, 100 Science Avenue, Zhengzhou, Henan, 450001, PR China. E-mail: Zzhongliang@outlook.com; Tel: +86 15810632393*

[b]*Institute of Chemistry, Henan Academy of Sciences, Zhengzhou, Henan, 450008, PR China*

acetamide center was thermodynamically more favorable under neutral conditions. Shi *et al.*[37] systematically explored the mechanisms by which H_2O, H_2O_2, NH_3, and their synergistic systems degrade A234 using DFT calculations. Their results demonstrated that NH_3, as an auxiliary nucleophile, significantly reduced the overall activation free energy, enabling nearly complete hydrolysis.

An ideal simulant should accurately replicate all relevant physicochemical properties of the target substance while exhibiting negligible acute toxicity. Simulant systems based on property characterization, physical adsorption, chemical degradation, and MOF degradation have been established for "classic" nerve agents, such as the G- and V-series.[38–40] In contrast, simulants for A-series nerve agents have not yet been widely investigated. Carvalho-Silva *et al.*[41] proposed GND1 as a simulant to mimic the mass spectrometric characteristics of A242. Santos *et al.*[42] introduced NTMGMP as a simulant for evaluating the efficacy of detoxifying agents against A242. Bernardo *et al.*[43] suggested 4-nitrophenyl (*E*)-*N*-(1-(diethylamino)-ethylidene)-P-methylphosphonamidatea (ANMP) as a simulant to assess the effectiveness of detoxifying agents for A230.

For hydrolysis simulants, it is essential to reproduce the hydrolysis pathways of the original substance and generate hydrolysis products that are identical or similar to those of the original substance. Although several studies have focused on the degradation of NAs in aqueous solutions, systematic investigations into their pH-dependent hydrolysis mechanisms are limited. In particular, the degradation mechanisms under acidic conditions and the development of corresponding hydrolysis simulants remain largely unexplored. To develop simulated nerve agents, the fluorine group is often replaced with a 4-nitrophenol group. For example, previous studies have used 4-nitrophenol as a leaving group to replace fluorine in NAs, producing simulants for toxicological evaluation.[42–45] In this study, the compounds with a fluorine group in A230, A232, and A234 were replaced with 4-nitrophenol to produce the following candidate hydrolysis simulants: ANMP, methyl (4-nitrophenyl) (*E*)-(1-(diethylamino)-ethylidene)phosphoramidate, and ethyl (4-nitrophenyl) (*E*)-(1-(diethylamino)-ethylidene)phosphoramidate. These simulants are structurally equivalent to NA and pesticide paraoxonhybrids and may retain some toxic properties. Phenol departs less readily than 4-nitrophenol but is superior to aliphatic alcohols; therefore, phenoxy-based scaffolds are also considered candidate hydrolysis simulants for phenyl (*E*)-*N*-(1-(diethylamino)ethylidene)-P-methylphosphonamidate (AMP), methyl phenyl (*E*)-(1-(diethylamino)-ethylidene)phosphoramidate, and ethyl phenyl (*E*)-(1-(diethylamino)-ethylidene)phosphoramidate. A PubChem substructure search (P(O)N=C(C)N, MW 200–300) identified ADPP (*N*′-diphenoxyphosphorylethanimidamide, PubChem CID 6252564) as a commercially available compound possessing the same P–N=C backbone and accessible toxicological data, rendering it an ideal candidate for this study (Fig. 1).

In this study, we combined thermodynamic methods and DFT calculations to investigate three A-series nerve agents (A230, A232, and A234) and seven potential hydrolysis simulant compounds. Protonation sites and dissociation constants were determined, Gibbs free energy changes were assessed, and hydrolysis mechanisms, reaction rates, and half-lives were predicted across a range of pH conditions. Suitable hydrolysis simulants were also identified through computational screening, and the reliability of the predictions was experimentally validated using hydrolysis studies of the selected simulants.

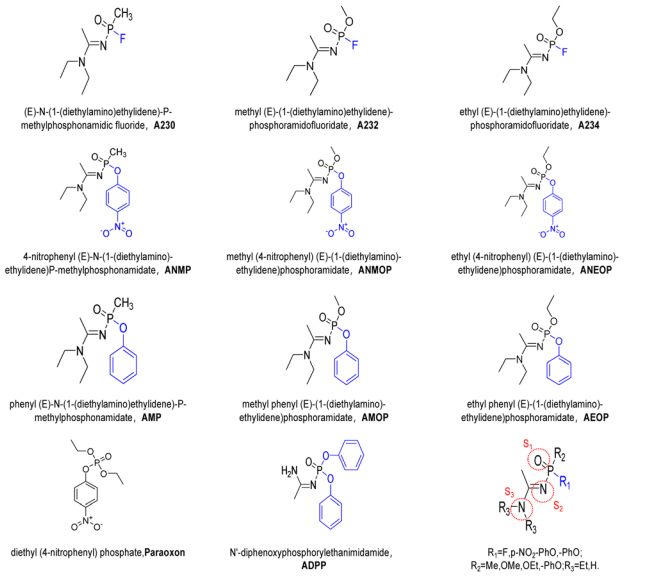

Fig. 1 NAs and simulants.

Experimental

Computational methods

Unless otherwise specified, all calculations were performed using the ORCA 6.0.1 program.[46] Molecular structures were initially pre-optimized at the GFN2-xTB level using the Goat functionality.[47,48] The 20 lowest-energy conformers were retained and subjected to further geometry optimization at the PCM(H_2O)/B3LYP[49]-D3(BJ)[50]/def2-SVP[51] level, followed by single-point energy calculations at the SMD[52](H_2O)/ωB97M-V[53]/def2-TZVPP[51] level. The lowest-energy conformation was kept for subsequent analysis. Diffuse functions (ma-def2-SVP/ma-def2-TZVPP) were applied under alkaline conditions.[54] All calculations were performed using Cartesian coordinates.

For reaction barrier calculations, geometry optimizations and intrinsic reaction coordinate (IRC) calculations were conducted consistently at the PCM(H_2O)/B3LYP-D3(BJ)/def2-SVP level for all systems to ensure a uniform baseline. Transition states were confirmed as first-order saddle points (with exactly one imaginary frequency) and validated by IRC calculations. Reactants and intermediates were verified as local minima (with no imaginary frequencies). Single-point energies were calculated at the SMD(H_2O)/ωB97M-V/def2-TZVPP level. For the dominant reaction pathways, additional higher-level single-point energy calculations were performed at the SMD(H_2O)/DLPNO-CCSD(T)[55]/def2-TZVPP level, employing the def2-TZVPP/C auxiliary basis set for electron correlation.

The "SlowConv" and "TightSCF" keywords were used to ensure convergence. All DFT calculations employed the RIJ-COSX method for acceleration.[56] The Coulomb integrals utilized the "def2/J" auxiliary basis set (or the "AutoAux" automatic selection under alkaline conditions). All other parameters were set to ORCA's default values.

For pK_a calculations, we followed the high-accuracy G4(MP2)-XP[57,58] protocol for gas-phase free energies. The solvation free energy was computed using the M05-2X/6-31G(d) method.

All molecular graphics were generated using Multiwfn[59,60] and VMD.[61]

pK_a determination. To assess the dissociation of the protonated nerve agent (AH^+) in aqueous solution, $AH^+ \rightleftharpoons A + H^+$, the p$K_a$ value was determined using eqn (1):[60,61]

$$pK_a = \frac{\Delta G^\circ_{aq}}{2.303RT} \quad (1)$$

where R is the universal gas constant, $T = 298.15$ K, and G°_{aq} is the standard Gibbs free energy change in deprotonation in aqueous solution, obtained using eqn (2):

$$\Delta G^\circ_{aq} = G^\circ_{aq}(A) + G^\circ_{aq}(H^+) - G^\circ_{aq}(AH^+) \quad (2)$$

$G^\circ_{aq}(X)$ (where X = A, H^+, or AH^+) represents the Boltzmann-weighted average over a set of conformers {C}. In this study, the 10 lowest-energy conformers were included:[62,63]

$$G^\circ_{aq}(X) = -RT \ln\left(\sum_{i\in\{C\}} e^{-G^\circ_{aq,i}(X)/RT}\right) \quad (3)$$

The aqueous-phase Gibbs free energy for each conformer, $G^\circ_{aq,i}(X)$, was computed as the sum of the gas-phase Gibbs free energy at 1 atm ($G^{1atm}_{gas,i}(X)$), the solvation free energy at a fixed concentration ($G^*_{solv,i}(X)$), and the free energy change for conversion from the gas-phase standard state (1 atm) to the solution standard state (1 M; 1.89 kcal mol^{-1}). $G^{1atm}_{gas,i}(X)$ was obtained using the high-accuracy G4(MP2)-XP composite method with ORCA. $G^*_{solv,i}(X)$ was calculated as the difference between the energy in water (SMD model) and the gas-phase energy, both of which were evaluated at the M05-2X/6-31G(d) level after geometry optimization as follows:

$$G^\circ_{aq,i}(X) = G^{1atm}_{gas,i}(X) + G^*_{solv,i}(X) + 1.89 \quad (4)$$

Half life calculation. For hydrolysis under fixed pH conditions, where the concentration of water or hydroxide ions effectively remains constant due to their significant excess compared with that of NAs, the reaction follows pseudo-first-order kinetics. The rate constant K_i (i = 1, 2, 3, 4) for each elementary step was estimated using transition state theory:[64,65]

$$K_i = \kappa\left(\frac{k_B T}{h}\right)\exp\left(\frac{-\Delta^\ddagger G_{aq}}{RT}\right) \quad (5)$$

where κ is the transmission coefficient estimated *via* the Skodje–Truhlar method,[66] k_B is the Boltzmann constant, T is the temperature in Kelvin, h is the Planck constant, $\Delta^\ddagger G_{aq}$ is the Gibbs activation energy in aqueous solution at 298.15 K, and R is the universal gas constant.

The overall pseudo-first-order rate constant khyd is as follows:

$$k_{hyd}\{A_{total}\} = \{AH^+\}[k_1\{H_2O\} + k_2\{OH^-\}] + \{A\}[k_3\{H_2O\} + k_4\{OH^-\}] \quad (6)$$

where $\{A_{total}\} = \{AH^+\} + \{A\}$is the total substrate concentration. Here, k_1 is the acid-catalyzed rate constant (*i.e.*, the reaction of protonated species AH^+ with water), k_2 is the specific base-catalyzed rate constant (*i.e.*, the reaction of protonated species AH^+ with OH^-), k_3 is the neutral hydrolysis rate constant (*i.e.*, the reaction of A with water), and k_4 is the base-catalyzed rate constant (*i.e.*, the reaction of A with OH^-). The concentration of $\{AH^+\}$can be expressed by the following formula, where K_a is the acid dissociation equilibrium constant of the protonated species AH^+, as determined by eqn (7):

$$\{AH^+\} = \frac{\{A\}\{H^+\}}{K_a} \quad (7)$$

Substituting eqn (7) into eqn (6) yields:

$$\begin{aligned} k_{hyd} &= \frac{\{A\}}{\{A\} + \frac{\{A\}\{H^+\}}{K_a}}\left[\frac{\{H^+\}[k_1\{H_2O\} + k_2\{OH^-\}]}{K_a} + k_3\{OH^-\} + k_4\{H_2O\}\right] \\ &= \left[\frac{\{H^+\}[k_1\{H_2O\} + k_2\{OH^-\}] + K_a[k_3\{H_2O\} + k_4\{OH^-\}]}{K_a + \{H^+\}}\right] \end{aligned} \quad (8)$$

The half life ($t_{1/2}$) of the pseudo-first-order reaction can be calculated as follows:

$$t_{1/2} = \frac{\ln 2}{k_{hyd}} \quad (9)$$

Preparation of ADPP

ADPP was synthesized according to a previously reported procedure.[67] Briefly, solutions of 0.05 M chloroacetamide in 20 mL of water and 0.05 M diphenyl phosphorochloridate in 60 mL of benzene were prepared. The two solutions were combined

under an ice bath, followed by the dropwise addition of 20 mL of a 10% NaOH aqueous solution. The reaction mixture was stirred in the ice bath for 1 h. Upon completion, the target product (ADPP) was isolated using standard workup procedures.

Characterization of ADPP

A stock solution of ADPP (10 mg mL^{-1}) was prepared in acetonitrile and stored at −20 °C. Working solutions (1 mg mL^{-1}) were obtained by diluting the stock solution with deionized water. The pH values were adjusted to 1, 3, 5, 9, 11, and 13 using the following buffers: 0.1 M HCl (pH 1), 0.1 M acetate (pH 3 and 5), 0.1 M carbonate/bicarbonate (pH 9 and 11), and 0.1 M KOH (pH 13).

The structure of ADPP was analyzed using high-performance liquid chromatography (HPLC) according to a previously reported method.[14] The mobile phase consisted of water containing 0.1% formic acid (solvent A) and acetonitrile (solvent B). The gradient elution program was set as follows: 10% B from 0 to 1 min, linearly increasing to 80% B at 6 min, holding for 0.5 min; then decreasing linearly to 10% B at 7 min and maintaining for 2 min. The flow rate was set at 0.3 mL min^{-1}. All HPLC experiments were performed using an autosampler with an injection volume of 5 μL.

Results and discussion

Simulants can mimic the specific physicochemical properties of chemical warfare agents (CWAs) without exerting high toxicity, and thus, play a critical role in CWA research. The use of simulants ensures experimental safety while preserving the scientific relevance of the investigations.[68,69] However, if a simulant is too similar to an agent, it may become highly toxic itself. Hence, compounds must be carefully selected based on the research objectives to achieve "relevant properties with controllable toxicity."

Protonation of NAs and simulants

Under low-pH conditions, protonation of the phosphate ester moiety markedly increases electrophilicity and concurrently reduces the hydrolytic activation barrier. However, NAs and simulants have three potential protonation sites ($S_{1,O-H^+}$, $S_{2,N1-H^+}$, and $S_{3,N2-H^+}$; Fig. 1), and protonation at each site has a distinct effect on the hydrolytic activation barrier and the final product.

Accurate mapping of the preferred protonation sites and their associated pK_a values is essential for elucidating acid-catalyzed degradation pathways. In this study, three potential protonation sites were systematically evaluated using the high-accuracy G4(MP2)-XP composite thermochemical method. The calculated pK_a values are listed in Table 1 and SI Table S1.

Typically, imine groups exhibit weaker basicity than tertiary amines and are less prone to protonation. However, the pK_a value corresponding to protonation at the imine nitrogen (S_2 site) in the NAs is significantly greater than those of the other protonation sites, which may be attributed to the unique structure of the amidino group. Similar to guanidine groups, amidino groups can form conjugated systems with partial aromaticity, increasing the susceptibility of the imine nitrogen to protonation. Consequently, all subsequent discussions regarding protonated species refer to protonation at the S2 site. Among the NAs, A230 exhibits a substantially higher pK_a value at the S_2 site than A232 and A234, indicating that A230 is more readily protonated under acidic conditions. This difference can be ascribed to the stronger electron-donating capacity of the methyl group at the *meta*-position of the amidino moiety in A230, relative to the methoxy group in A232 and the ethoxy group in A234.

The pK_a values of the simulants protonated at the $S_{2,N1-H+}$ site are summarized in Table 2 and SI Table S2. For simulants with phenol or 4-nitrophenol as the leaving group, the trend in pK_a values is consistent with that of the corresponding NAs, though the absolute values are greater. In contrast, the pK_a value of ADPP is closest to that of the actual NAs, suggesting that its protonation behavior can more accurately replicate their acid-catalyzed characteristics.

LEAE of NAs and simulants

Nucleophilic reagents can approach the phosphorus atom in NAs from multiple spatial directions, and the preferred reaction site dictates the magnitude of the activation barrier. In this study, Local Electron Attachment Energy (LEAE) analysis was used to evaluate the nucleophilic reaction sites and their reactivities with the NAs and simulants. A more negative LEAE value denotes a stronger electrophilic character, as well as greater susceptibility to nucleophilic attack in the absence of external factors that hinder it, such as steric hindrance.

The calculated LEAE results for the NAs are presented in Fig. 2, and those for the simulants are shown in SI Fig. S1. NAs contain two electrophilic centers: the phosphorus atom and the carbon atom of the amidine group. Given the poor leaving-group ability of substituents attached to the amidine carbon and the absence of reported hydrolysis products initiated at this

Table 1 Dissociation constants of different protonation sites in NAs

Protonated agent	$S_{1,O-H^+}$	$S_{2,N1-H^+}$	$S_{3,N2-H^+}$
A230-H^+	−3.46	3.24	−5.68
A232-H^+	−5.10	1.74	−6.99
A234-H^+	−5.39	1.89	−6.77

Table 2 Dissociation constants of simulants protonated at the S_2 (N_1–H^+) site

Protonated agent	$S_{2,N1-H^+}$	Protonated agent	$S_{2,N1-H^+}$
AMP-H^+	4.89	ANMP-H^+	4.74
AMOP-H^+	2.43	ANMOP-H^+	2.96
AEOP-H^+	3.25	ANEOP-H^+	3.17
ADPP-H^+	2.28		

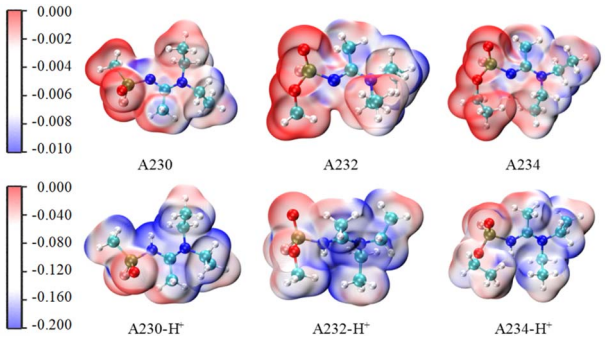

Fig. 2 Local electron attachment energy (LEAE) of the NAs-unit: eV.

carbon in existing experimental literature,[14,33] the discussion focused exclusively on phosphorus nucleophilic substitution. Regardless of protonation status, the order of electrophilicity strength among the NAs remained consistent: A230 > A232 > A234, indicating that A230 is the most susceptible to nucleophilic attack. A similar trend was observed for the simulants. Notably, this electrophilicity order was inverse to the electron-withdrawing capacities of their side-chain groups (methoxy > ethoxy > methyl).

For compounds bearing identical side-chain substituents, the LEAE at the phosphorus atom decreased in the order: fluorine > 4-nitrophenoxy > phenoxy, which aligns with the electron-withdrawing abilities of these leaving groups. Methoxy and ethoxy groups acted as flexible substituents whose terminal atoms spontaneously adopted energetically favorable conformations due to influences from charge distribution and steric hindrance, thereby modulating the LEAE values around the phosphorus atom. In both NAs and simulants, the spatial point of minimum LEAE near the phosphorus atom is located at the *para*-position relative to strong electron-withdrawing groups. In the non-protonated state, this minimum consistently resides at the *para*-position of the leaving group, suggesting a greater propensity for nucleophilic attack at this site. After protonation, electrophilicity is significantly enhanced, and the minimum shifts to the *para*-position of the protonated imine group.

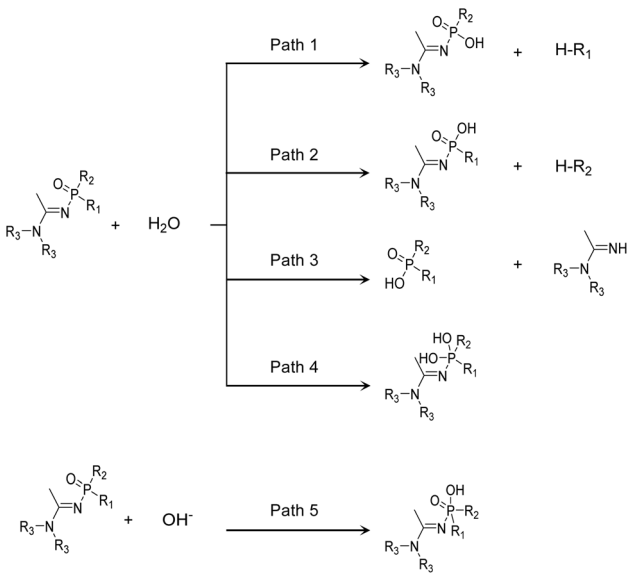

Fig. 3 Hydrolysis pathways of non-protonated NAs and simulants. R_1 = F, p-NO_2-PhO, –PhO; R_2 = Me, OMe, OEt, –PhO; R_3 = Et, H.

Hydrolysis mechanisms of non-protonated species

The degradation mechanisms of NAs by water and hydroxide ions were investigated. In the initial reaction stage, five possible reaction pathways were considered (Fig. 3). Paths 1–4 describe the nucleophilic attack of a water molecule on the phosphorus center, accompanied by proton transfer to four different adjacent atoms. Path 5 involves direct nucleophilic attack by a hydroxide ion on the phosphorus atom. In paths 1–4, solvent-assisted proton transfer significantly reduces the reaction energy barrier (SI Table S3), a finding consistent with previously reported results.[37] Unless otherwise stated, all subsequent energy barriers for water-mediated reactions refer to those involving solvent-assisted proton transfer. Based on the reaction sites identified *via* LEAE calculations, the Gibbs free energy barriers for the hydrolysis pathways of non-protonated NAs are summarized in Table 3.

Among the possible pathways for direct reactions between NAs and water, Path 4, in which a water molecule attacks the phosphorus atom from the *para*-position relative to the fluorine atom (an S_N2 mechanism) and transfers a proton to the phosphoryl oxygen, exhibits a lower Gibbs free energy barrier than Paths 1–3. Although solvent assistance slightly reduces the barrier, it remains higher than 36 kcal mol^{-1}. In contrast, Path 5, involving nucleophilic attack by hydroxide ions, exhibits a Gibbs free energy barrier of <18 kcal mol^{-1}, which is significantly lower than that of water-mediated pathways. Applying a threshold of 22.7 kcal mol^{-1} to determine whether a reaction readily occurs at room temperature,[70] it is concluded that hydrolysis of NAs by water is unlikely under neutral conditions, whereas reaction with hydroxide ions proceeds rapidly under alkaline conditions. These computational results align with previously reported experimental observations.[35]

The Gibbs free energy barriers for the dominant hydrolysis pathways (Paths 4 and 5) of non-protonated NAs and their simulants are summarized in Table 4. The energy barriers for the simulants are slightly greater than those of the corresponding NAs. Among the simulants, those with a 4-nitrophenoxy leaving group present lower energy barriers than those with a phenoxy leaving group, reflecting the superior leaving ability of 4-nitrophenolate. The energy barriers calculated using the DLPNO-CCSD(T) and ωB97M-V methods exhibit consistent trends, with deviations of <10%.

Table 3 Gibbs free energy barriers (kcal mol^{-1}) for different reaction pathways of non-protonated NAs

Agent	Path 1	Path 2	Path 3	Path 4	Path 5
A230	52.46	91.73	33.57	36.80	16.42
A232	56.20	47.79	37.03	37.03	17.01
A234	56.08	45.35	37.33	36.82	17.07

Table 4 Gibbs free energy barriers (kcal mol^{-1}) for the dominant hydrolysis pathways of non-protonated NAs and simulants

	Path 4		Path 5	
Agent	ωB97M-V	DLPNO-CCSD(T)	ωB97M-V	DLPNO-CCSD(T)
A230	36.80	40.09	16.42	17.53
A232	37.03	40.50	17.01	18.34
A234	36.82	40.25	17.07	18.39
AMP	39.11	42.75	19.65	20.52
AMOP	52.1	50.06	19.67	20.92
AEOP	42.87	46.25	20.15	21.30
ADPP	37.86	40.74	19.85	20.78
ANMP	35.86	39.38	16.66	17.64
ANMOP	44.41	47.58	18.67	20.33
ANEOP	41.51	45.41	18.44	19.77

Hydrolysis mechanisms of protonated NAs

The high hydrolysis energy barriers of non-protonated NAs do not explain the experimental observation that NAs degrade rapidly, even under strongly acidic conditions. In this section, the degradation mechanisms of protonated NAs (A230-H^+, A232-H^+, and A234-H^+) by water and hydroxide ions were investigated. In the initial reaction stage, six possible reaction pathways were systematically analyzed (Fig. 4). Paths 6–9 involve nucleophilic attack by a water molecule on the phosphorus atom of protonated NAs, accompanied by proton transfer to various adjacent atoms. Water-assisted proton transfer also reduces the energy barriers in these pathways. Previous studies have suggested that phosphonates may undergo pre-equilibrium proton transfer, leading to deprotonation of the nucleophile, followed by hydroxide attack on the

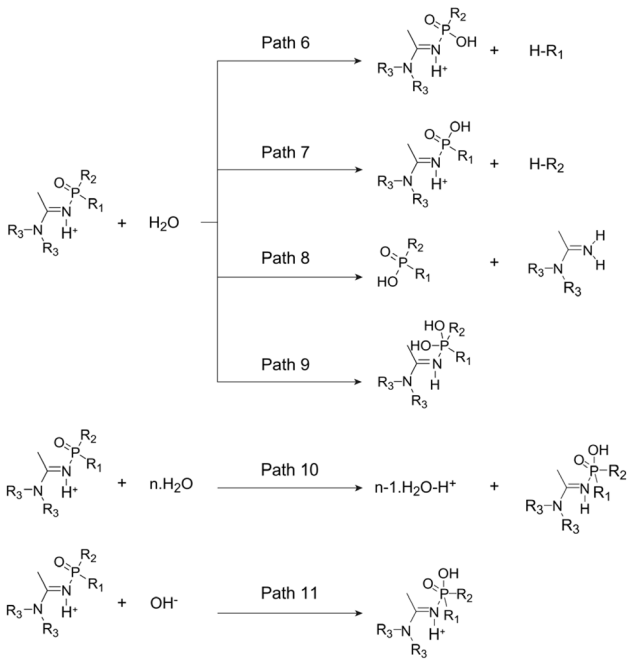

Fig. 4 Hydrolysis pathways of protonated NAs and simulants. R_1 = F, p-NO_2-PhO, –PhO; R_2 = Me, OMe, OEt, –PhO; R_3 = Et, H.

Table 5 Gibbs free energy barriers for different reaction pathways of protonated NAs

Protonated agent	Path 6	Path 7	Path 8	Path 9	Path 10	Path 11
A230-H^+	40.35	74.39	38.49	29.00	19.55	11.80
A232-H^+	40.73	34.06	42.61	26.20	18.91	9.76
A234-H^+	42.68	35.65	43.95	27.15	21.91	9.71

protonated phosphonate.[71,72] Although ground-state proton transfer from water to phosphonate is generally associated with high energy barriers and is thus unlikely, it has been reported that the dominant pathway for water attack on protonated hexamethylphosphoramide (HMPA) involves proton transfer between water molecules, with hydroxide subsequently attacking the protonated HMPA.[64] Inspired by this mechanism, Path 10, describing water molecules attacking protonated NAs through proton transfer, was further investigated. Path 11 involves direct nucleophilic attack by a hydroxide ion on the phosphorus atom of protonated NAs. Based on pK_a and LEAE calculations, the Gibbs free energy barriers for the initial hydrolysis steps of protonated NAs are summarized in Table 5.

A comparison between Tables 5 and 3 revealed that protonation significantly reduced the energy barrier for reactions between the NAs and water/hydroxide ions, corroborating the LEAE results, which indicate that protonation enhances the electrophilicity of the phosphorus center and promotes nucleophilic attack. Notably, the order of energy barriers for the dominant pathways of protonated NAs (Paths 9, 10, and 11) differed from the trend observed for non-protonated species, where A230 generally presented lower barriers than A232 and A234. This difference may arise from the interplay of multiple factors. Under non-protonated conditions, steric effects predominate, resulting in lower energy barriers for A230 (with a methyl side chain) than those for A232 and A234 (with longer side chains). After protonation, the significantly enhanced electrophilicity amplifies the electron-donating effect of the methyl group in A230, resulting in higher energy barriers for its dominant pathways than A232 and A234.

The Gibbs free energy barriers for the dominant hydrolysis pathways (Paths 9, 10, and 11) of protonated NAs and their simulants are summarized in Table 6. The energy barriers for the simulants were slightly greater than those of the corresponding NAs. Among the simulants, those with a 4-nitrophenoxy leaving group presented lower energy barriers than those with a phenoxy leaving group. The protonated form of ADPP demonstrated energy barriers closer to those of the NAs, indicating its superior performance as a simulant under acidic conditions.

Based on the identified dominant hydrolysis pathways for protonated and non-protonated NAs, possible reaction products were further explored (Fig. 5).

For nonprotonated NAs, fluorine serves as a relatively good leaving group with significantly greater leaving ability than other substituents attached to phosphorus. Thus, the fluorine departure step has a low energy barrier, and the rate-

Table 6 Gibbs free energy barriers for the dominant hydrolysis pathways of protonated NAs and simulants

	Path 9		Path 10		Path 11	
Protonated agent	ωB97M-V	DLPNO-CCSD(T)	ωB97M-V	DLPNO-CCSD(T)	ωB97M-V	DLPNO-CCSD(T)
A230-H$^+$	29.00	32.38	19.55	21.90	11.80	12.95
A232-H$^+$	26.20	30.54	18.91	21.90	9.76	10.83
A234-H$^+$	27.15	31.41	21.91	22.08	9.71	10.84
AMP-H$^+$	33.12	35.59	23.52	25.86	13.44	14.23
AMOP-H$^+$	33.02	36.65	24.41	27.13	12.91	13.81
AEOP-H$^+$	34.01	37.71	27.44	30.94	13.51	14.36
ADPP-H$^+$	26.08	28.97	19.23	21.72	12.41	13.04
ANMP-H$^+$	32.67	35.88	23.03	25.55	12.21	12.84
ANMOP-H$^+$	29.52	33.39	26.05	29.55	13.96	15.17
ANEOP-H$^+$	30.83	34.92	25.99	28.77	12.68	13.68

determining step (RDS) precedes the nucleophilic attack. Hydroxide ions can undergo S_N2 attack at the *para*-position relative to fluorine, with the RDS being the actual nucleophilic attack. The detachment step when leaving the group has a lower energy barrier and may even co-occur with the nucleophilic attack of hydroxide ions. In reactions with water, a direct attack on the P–F bond is less favorable due to its length and electronic environment. Instead, the dominant pathway involves an initial water attack on the phosphoryl oxygen (P═O), followed by the departure of fluorine.

For protonated NAs, protonation induces deprotonation of surrounding water molecules, and the resulting hydroxide ions attack the protonated NAs, forming the same intermediate as in the direct hydroxide attack. The RDS for both pathways is the nucleophilic attack on protonated NA. Both the fluorine group and the protonated amidine moiety are prone to leaving, with similar energy barriers for decomposition (SI Fig. S2). The intermediate can decompose *via* P–F or P–N cleavage, which may explain the formation of amidine byproducts in NA hydrolysis experiments under neutral conditions.[14,33] The results (SI Fig. S2) showed that the dominant product of protonated A230 was P–N cleavage, while the dominant product of protonated A232 and A234 was P–F cleavage.

Predicted reaction rates and half-lives

Building on the dominant pathways identified under different conditions, the corresponding Gibbs free energy barriers were corrected for free energy changes and reactant concentrations. These values were then substituted into the rate constant (eqn (5)–(8)) to determine the reaction rates. The half-lives were calculated using eqn (9). The concentration of the NAs was set to

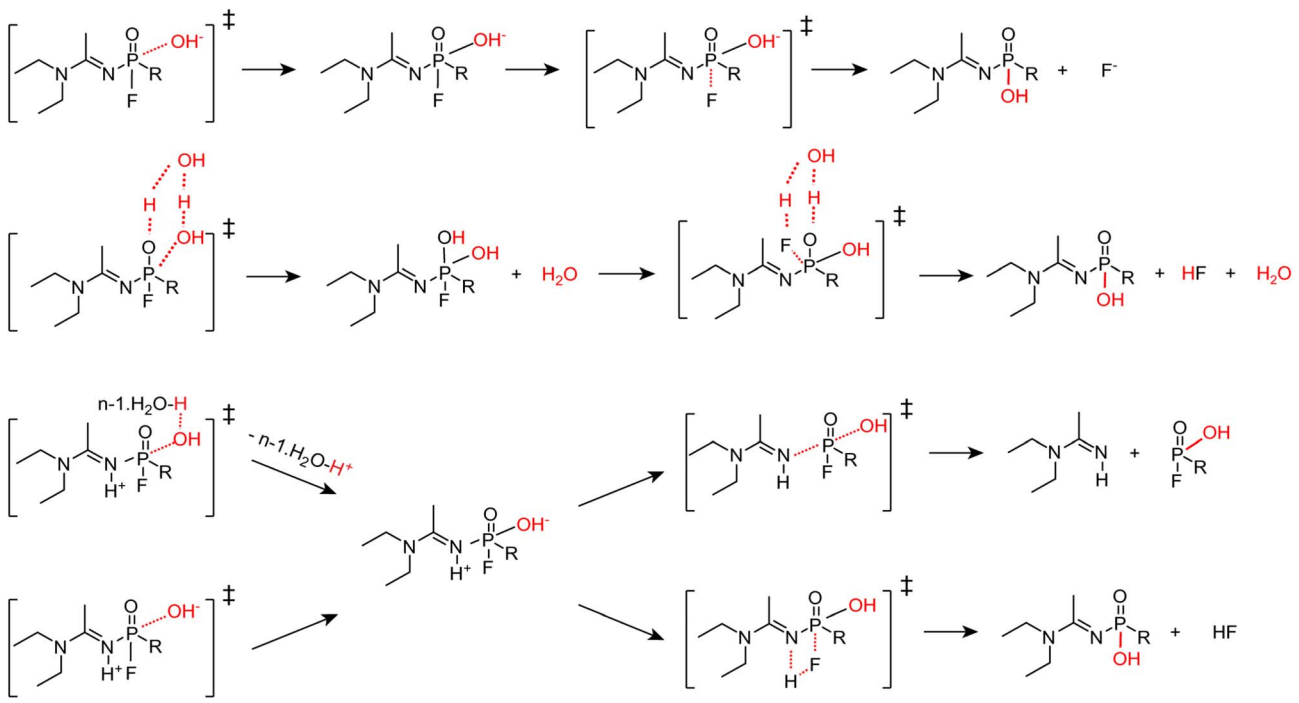

Fig. 5 Dominant hydrolysis reaction pathways of the NAs, R = Me, OMe, OEt.

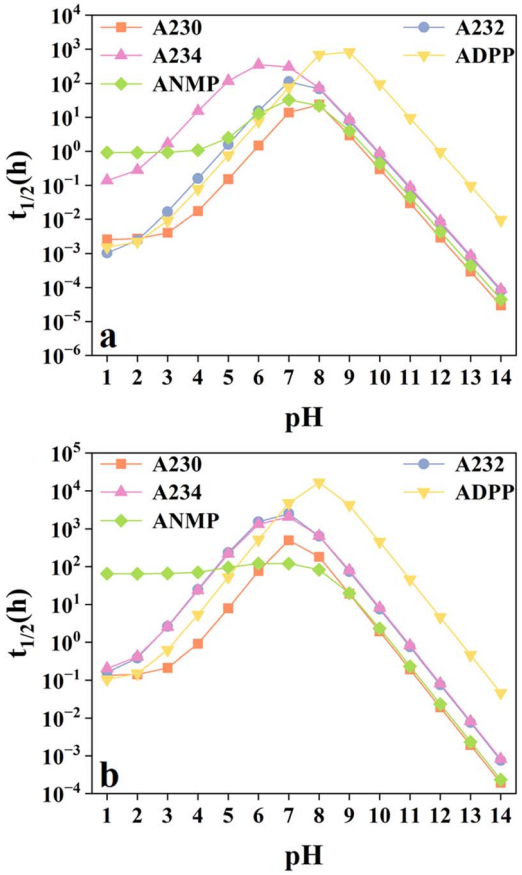

Fig. 6 Predicted half-lives ($t_{1/2}$) *via* two computational methods. (a) ωB97M-V/def2-TZVPP; (b) DLPNO-CCSD(T)/def2-TZVPP.

20 mM, a value consistent with those commonly used in the literature.[33] In contrast, the concentration of water was set to 55.6 M. By comparing the reaction rates and half-lives across various pH conditions, two simulants, ADPP and ANMP, were identified as most closely replicating the hydrolysis characteristics of the NAs (SI Fig. S3 and 6).

Calculations at the ωB97M-V level revealed significant differences in the half-lives of the NAs under neutral and acidic conditions, following the order A234 > A232 > A230. Under alkaline conditions, the differences among the three compounds diminished. The half life of ADPP under neutral and acidic conditions was comparable to that of A232, whereas it exceeded that of all the other NAs under alkaline conditions. For ANMP, the pH-dependent trend in the half life under acidic conditions differed from that of the NAs, though its half life under neutral and alkaline conditions was similar to that of A230.

DLPNO-CCSD(T) calculations predicted comparable half-lives for A234 and A232, with the overall order being A234 ≈ A232 > A230. The half life of ADPP under neutral and acidic conditions fell between those of A230 and A232, while it was longer than those of the NAs under alkaline conditions. ANMP again exhibited a pH-dependent trend inconsistent with that of the NAs under neutral and acidic conditions, though its half life under alkaline conditions was similar to that of A230.

The energy barriers calculated *via* DLPNO-CCSD(T) were generally greater than those calculated *via* ωB97M-V, resulting in correspondingly longer predicted half-lives. Nevertheless, both methods produced consistent overall trends in pH-dependent half life variation. Given the generally higher theoretical accuracy of the DLPNO-CCSD(T) method, the reaction rates and half-lives in this study were predicted based on energy barriers obtained at this level (Fig. 7).

The potential hydrolysis mechanisms and activation free energies of the NAs and the simulants ADPP and ANMP in aqueous solutions were computationally evaluated and compared. As the pH increased, the hydrogen ion concentration and proportion of protonated species gradually decreased in the advantageous reaction pathway Path 10, catalyzed by acid, causing the reaction rate to first plateau and then decline. According to eqn (8), the rate of acid-catalyzed hydrolysis remained approximately constant when the acid dissociation constant K_a of the protonated species was much smaller than the hydrogen ion concentration. Owing to its relatively high pK_a (4.74), ANMP exhibited a nearly constant acid-catalyzed rate in the pH range of 1–4. The other NAs and simulants maintained stable reaction rates only under strongly acidic conditions.

In the base-catalyzed dominant pathway (Path 5), the reaction rate increased gradually with rising pH, driven by the increasing concentration of hydroxide ions and the growing proportion of deprotonated species. When the pH increased to the point where $K_a \gg [H^+]$, indicating the dominance of deprotonated species, the reaction rate became directly proportional solely to the hydroxide ion concentration. For the acid-base catalyzed dominant pathway (Path 11), the reaction rate was proportional to the concentrations of both hydroxide ions and the protonated species. When $K_a \ll [H^+]$, the rate increased with rising hydroxide concentration. Conversely, when $K_a \gg [H^+]$, the reaction rate remained constant. The uncatalyzed hydrolysis pathway (Path 4) exhibited the highest reaction energy barrier, indicating that its contribution to the overall hydrolysis rate was negligible across the entire pH range. Under acidic conditions, the total reaction rate was predominantly governed by acid-catalyzed pathways.

Under alkaline conditions, base-catalyzed pathways became the dominant ones. Within the neutral pH region, acid catalysis, base catalysis, and concerted acid–base catalysis operated in combination, whereas the contribution from uncatalyzed neutral hydrolysis remained insignificant throughout all pH conditions.

Overall, the hydrolysis of NAs and the simulants ADPP and ANMP was strongly influenced by pH and the fraction of protonated species, resulting in a characteristic "inverted bell-shaped" pH profile. The pH-dependent hydrolysis rate curve of ADPP closely resembled that of the NAs, with its rate falling between neutral and acidic intermediate conditions, as indicated by A230 and A232. However, it hydrolyzed more slowly than the NAs under alkaline conditions. ANMP exhibited hydrolysis rates closer to those of the NAs under alkaline conditions. ANMP are structurally equivalent to hybrids of NAs and the pesticide paraoxon and may still retain specific toxic properties. Considering the potential toxicity concerns, this

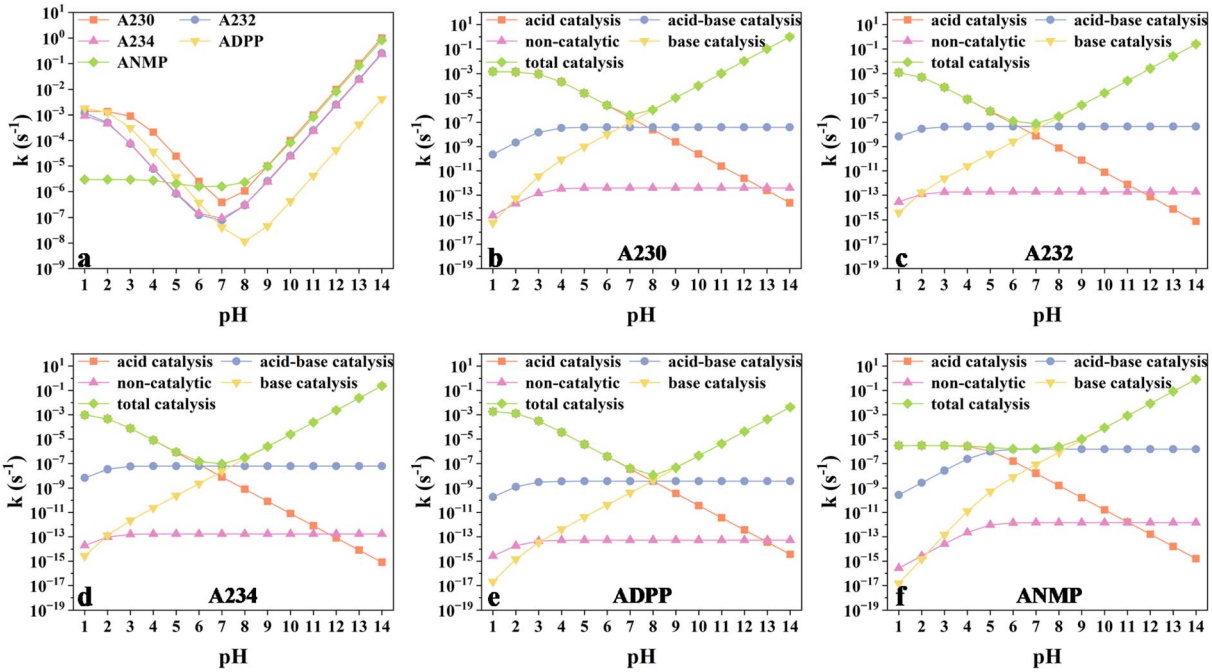

Fig. 7 Predicted reaction rates (k) of the NAs and simulants across pH values. (a) Total reaction rates (k) of the NAs and simulants; (b–f) reaction rates (k) of different reaction paths.

study utilized the less toxic ADPP simulator to conduct hydrolysis tests, thereby validating the accuracy of computational simulations.

As indicated by eqn (5), (8), and (9), the half-lives were highly sensitive to changes in both the reaction energy barriers and the K_a values. A difference of only 1.36 kcal mol^{-1} in the energy barrier can lead to an order-of-magnitude change in K_a. It is widely accepted that an error in Gibbs free energy barriers of <2 kcal mol^{-1} (corresponding to an error in the reaction rate of 1–2 orders of magnitude) is acceptable in DFT calculations of aqueous-phase reactions.[43] However, achieving greater accuracy requires methods beyond standard DFT. In this study, the more accurate G4(MP2)-XP method was used to calculate dissociation constants, and DLPNO-CCSD(T) was employed for single-point energy calculations. Notably, the hydrolysis products of phosphonate esters may alter the solution pH, and other ions present could also influence the reaction. Even high-level computations reduce but do not eliminate errors, making exact agreement between experimental and computed half-lives challenging to achieve.

To validate the computational predictions, experimental hydrolysis studies of ADPP were conducted at various pH values. At pH levels of 1, 3, 5, 7, 9, 11, and 13, the experimental values exhibited trends consistent with those predicted by both the ωB97M-V and DLPNO-CCSD(T) methods. The absolute values were closer to those obtained with the more accurate DLPNO-CCSD(T) method. Thus, the hydrolysis experimental data for ADPP generally support the reliability of the chosen computational methods and results. Future studies should further explore the optimal conditions for degrading the simulants ADPP and ANMP to minimize potential risks to human health and the environment (Fig. 8).

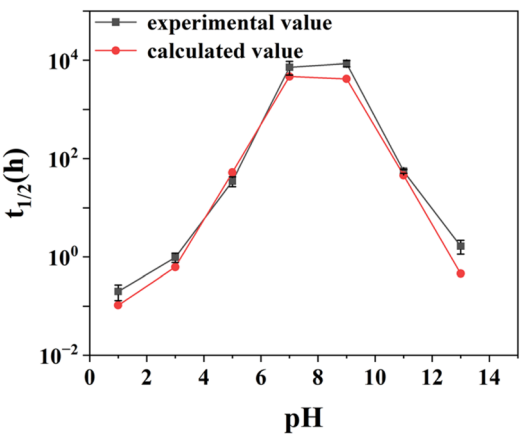

Fig. 8 Predicted and experimental half-lives ($t_{1/2}$) of ADPP.

Conclusion

The hydrolysis mechanisms of NAs under different pH conditions were systematically investigated using theoretical calculations. Under acidic conditions, the dominant hydrolysis pathway involved protonated NAs inducing the deprotonation of surrounding water molecules, followed by nucleophilic attacks on protonated species (Path 10). Under alkaline conditions, an S_N2-type attack by hydroxide ions at the *para*-position relative to the fluorine atom (Path 5) was predominant. Under neutral conditions, Paths 5, 10, and 11 collectively contributed to hydrolysis, with the latter involving hydroxide attack at the

para-position of the protonated imine nitrogen. Influenced by both acid and base catalysis, the hydrolysis half life of the NAs exhibited a characteristic bell-shaped curve as a function of pH. Hydrolysis byproducts may originate from reactions between protonated NAs and water or hydroxide ions (Paths 10 and 11), with comparable energy barriers for P–F and P–N cleavage in the resulting intermediates. ADPP and ANMP were identified as suitable hydrolysis simulants based on the computational results, and the accuracy of the calculations was verified through ADPP hydrolysis experiments. These findings not only deepen our understanding of NA hydrolysis but also provide a theoretical foundation and candidate simulants for the development of low-toxicity and high-efficiency detoxifying agents against A-series nerve agents.

Author contributions

Junjun Jia: conceptualization, methodology, investigation, data collection, writing-original draft preparation, writing – review & editing, validation. Wenjie Duan: data collection, visualization. Qingyuan Li: data collection. Xinxin Xu: preparation, data collection and analysis. Zhenbang Tian: investigation. Zhongliang Zhang: investigation, writing – original draft preparation.

Conflicts of interest

The authors declare that they have no known competing financial interests or personal relationships that could have appeared to influence the work reported in this paper.

Data availability

All data generated or analyzed during this study are included in this published article and its supplementary information (SI) files. Supplementary information: (1) additional computational details; (2) Cartesian coordinates for all optimized structures reported in the study. See DOI: https://doi.org/10.1039/d5ra09488g.

Acknowledgements

This work was supported by the Henan Provincial Science and Technology Research Project (grant no. 242102321056), the Joint Fund of Henan Province Science and Technology R&D Program (grant no. 225200810028), the Basic Research Project of Henan Academy of Sciences (grant no. 240603068), and the Key International Science and Technology CoFfioperation Project in Henan Province (grant no. 231111520400).

References

1 L. V. J. van Melis, H. J. Heusinkveld, C. Langendoen, A. Peters and R. H. S. Westerink, Organophosphate insecticides disturb neuronal network development and function via non-AChE mediated mechanisms, *Neurotoxicology*, 2023, **94**, 35–45, DOI: 10.1016/j.neuro.2022.11.002.

2 E. Nepovimova and K. Kuca, The history of poisoning: From ancient times until modern ERA, *Arch. Toxicol.*, 2019, **93**, 11–24, DOI: 10.1007/s00204-018-2290-0.

3 B. Wiaderek, M. Wiśnik-Sawka, D. Gajda, K. Rzadkowska, P. Bryczek-Wróbel and T. Sałaciński, 4th generation of warfare agents—Novichoks: Threats, problems, challenges for the security of the armed forces and civilian population, *Food Chem. Toxicol.*, 2025, **200**, 115371, DOI: 10.1016/j.fct.2025.115371.

4 J. Opravil, J. Pejchal, V. Finger, J. Korabecny, T. Rozsypal, M. Hrabinova, L. Muckova, V. Hepnarova, J. Konecny, O. Soukup and D. Jun, A-agents, misleadingly known as "Novichoks": A narrative review, *Arch. Toxicol.*, 2023, **97**, 2587–2607, DOI: 10.1007/s00204-023-03571-8.

5 R. Puglisi, R. Santonocito, A. Pappalardo and G. Trusso Sfrazzetto, Smart sensing of nerve agents, *ChemPlusChem*, 2024, **89**, e202400098, DOI: 10.1002/cplu.202400098.

6 N. A. H. Thiermann and F. Worek, *Treatment of Nerve Agent*, The Royal Society of Chemistry, 2016, vol 2, pp. 1–42.

7 M. Labaška, M. Gál, T. Mackuľak, J. Švorec, J. Kučera, J. Helenin, V. Svitková and J. Ryba, Neutralizing the threat: A comprehensive review of chemical warfare agent decontamination strategies, *J. Environ. Chem. Eng.*, 2024, **12**, 114243, DOI: 10.1016/j.jece.2024.114243.

8 V. S. Mirzayanov, Dismantling the soviet/Russian chemical weapons complex: An insider's view, in *Chemical Weapons Disarmament in Russia: Problems and Prospects*, 1995, pp. 21–33.

9 J. Stewart, The grey orchestra, *Russ. J.*, 2022, **167**, 38–49, DOI: 10.1080/03071847.2022.2075117.

10 J. D. Haslam, P. Russell, S. Hill, S. R. Emmett and P. G. Blain, Chemical, biological, radiological, and nuclear mass casualty medicine: A review of lessons from the Salisbury and Amesbury Novichok nerve agent incidents, *Br. J. Anaesth.*, 2022, **128**, e200–e205, DOI: 10.1016/j.bja.2021.10.008.

11 D. Steindl, W. Boehmerle, R. Körner, D. Praeger, M. Haug, J. Nee, A. Schreiber, F. Scheibe, K. Demin, P. Jacoby, R. Tauber, S. Hartwig, M. Endres and K.-U. Eckardt, Novichok nerve agent poisoning, *Lancet*, 2021, **397**, 249–252, DOI: 10.1016/S0140-6736(20)32644-1.

12 M. Noga and K. Jurowski, What do we currently know about Novichoks? The state of the art, *Arch. Toxicol.*, 2023, **97**, 651–661, DOI: 10.1007/s00204-022-03437-5.

13 H. Bhakhoa, L. Rhyman and P. Ramasami, Theoretical study of the molecular aspect of the suspected novichok agent A234 of the Skripal poisoning, *R. Soc. Open Sci.*, 2019, **6**, 181831, DOI: 10.1098/rsos.181831.

14 J. Y. Lee, K. C. Lim and H. S. Kim, Characterization and study on fragmentation pathways of a novel nerve agent "novichok (A234)" in aqueous solution by liquid chromatography-tandem mass spectrometry, *Molecules*, 2021, **26**, 1059, DOI: 10.3390/molecules26041059.

15 E. Szliszka, Z. P. Czuba, M. Domino, B. Mazur, G. Zydowicz and W. Krol, Ethanolic extract of propolis (EEP) enhances the apoptosis- inducing potential of TRAIL in cancer cells, *Molecules*, 2009, **14**, 738–754, DOI: 10.3390/molecules.

16 M. Eskandari, S. M. Faraz, S. E. Hosseini, S. Moradi and H. Saeidian, Fragmentation pathways of chemical weapons convention-related organophosphorus Novichok agents: The electron ionization and electrospray ionization tandem mass spectroscopy and DFT calculation studies, *Int. J. Mass Spectrom.*, 2022, **473**, 116794, DOI: 10.1016/j.ijms.2021.116794.

17 H. Kim, U. H. Yoon, T. I. Ryu, H. J. Jeong, S. il Kim, J. Park, Y. S. Kye, S.-R. Hwang, D. Kim, Y. Cho and K. Jeong, Calculation of the infrared spectra of organophosphorus compounds and prediction of new types of nerve agents, *New J. Chem.*, 2022, **46**, 8653–8661, DOI: 10.1039/D2NJ00850E.

18 M. Otsuka, A. Yamaguchi and H. Miyaguchi, Analysis of degradation products of Novichok agents in human urine by hydrophilic interaction liquid chromatography–tandem mass spectrometry, *Forensic Toxicol.*, 2023, **41**, 221–229, DOI: 10.1007/s11419-022-00656-4.

19 M. Chalaris and A. Koufou, Antoine equation coefficients for novichok agents (A230, A232, and A234) via Molecular Dynamics simulations, *Physchem*, 2023, **3**, 244–258, DOI: 10.3390/physchem3020017.

20 M. Otsuka, A. Yamaguchi and H. Miyaguchi, Simultaneous analysis of degradation products of Novichok agents and conventional nerve agents in human urine by ion chromatography-tandem mass spectrometry using ammonium regeneration solution, *J. Chromatogr. A*, 2023, **1707**, 464290, DOI: 10.1016/j.chroma.2023.464290.

21 D. Sarkar, A. Das and S. Naha, Smart tool for novichok: A concise review on real-time detection techniques, *Monatsh. Chem.*, 2023, **154**, 673–682, DOI: 10.1007/s00706-023-03087-y.

22 M. Chalaris and A. Koufou, A study of thermodynamic and transport properties of Novichok agents (A230, A232, A234) via molecular dynamics simulations: Insights into Mirzayanov's proposed structures, *Comput. Theor. Chem.*, 2024, **1236**, 114584, DOI: 10.1016/j.comptc.2024.114584.

23 E. Tafaki and M. Chalaris, Investigating QSAR models for Chemical Warfare Agents: Biological, Biochemical, and Environmental Perspectives, *WSEAS Trans. Biol. Biomed.*, 2024, **21**, 281–301, DOI: 10.37394/23208.2024.21.29.

24 P. Novak, electronic structure of chemical warfare agents, *J. Electron Spectrosc. Relat. Phenom.*, 2025, **279**, 147523, DOI: 10.1016/j.elspec.2025.147523.

25 T. C. C. Franca, D. A. S. Kitagawa, S. F. A. Cavalcante, J. A. V. da Silva, E. Nepovimova and K. Kuca, Novichoks: The dangerous fourth generation of chemical weapons, *Int. J. Mol. Sci.*, 2019, **20**, 1222, DOI: 10.3390/ijms20051222.

26 A. S. Cornelissen, R. M. van den Berg, J. P. Langenberg, M. van Grol, R. Bross, J. Pittman, L. Cochrane and V. Savransky, Effective skin decontamination with RSDL® (reactive skin decontamination lotion kit) following dermal exposure to a Novichok class nerve agent, *Chem. Biol. Interact.*, 2024, **395**, 111001, DOI: 10.1016/j.cbi.2024.111001.

27 H. Jung, J. Heo, N. Park, K. C. Lim, H. Jung, V. Do Cao and S. Joung, Elimination of A-234 from the environment: Effect of different decontaminants, *J. Hazard. Mater.*, 2023, **451**, 131150, DOI: 10.1016/j.jhazmat.2023.131150.

28 T. Rozsypal, Persistence of A-234 nerve agent on indoor surfaces, *Chemosphere*, 2024, **357**, 141968, DOI: 10.1016/j.chemosphere.2024.141968.

29 P. R. Chai, B. D. Hayes, T. B. Erickson and E. W. Boyer, Novichok agents: A historical, current, and toxicological perspective, *Toxicol. Commun.*, 2018, **2**, 45–48, DOI: 10.1080/24734306.2018.1475151.

30 M. Hrabinova, J. Pejchal, V. Hepnarova, L. Muckova, L. Junova, J. Opravil, J. Zdarova Karasova, T. Rozsypal, A. Dlabkova, H. Rehulkova, T. Kucera, Z. Vecera, F. Caisberger, M. Schmidt, O. Soukup and D. Jun, A-series agent A-234: Initial in vitro and in vivo characterization, *Arch. Toxicol.*, 2024, **98**, 1135–1149, DOI: 10.1007/s00204-024-03689-3.

31 V. S. Mirzaynov, *State Secrets: an Insider's Chronicle of the Russian Chemical Weapons Program*, Outskirts Press, Inc, 2008.

32 B. Smolkin, V. Nahum, E. Bloch-Shilderman, U. Nili, G. Fridkin and N. Ashkenazi, Acetohydroxamic acid salts: Mild, simple and effective degradation reagents to counter Novichok nerve agents, *RSC Adv.*, 2024, **14**, 14904–14909, DOI: 10.1039/d4ra02038c.

33 M. C. de Koning, C. Vieira Soares, M. van Grol, R. P. T. Bross and G. Maurin, Effective degradation of novichok nerve agents by the zirconium metal–organic framework MOF-808, *ACS Appl. Mater. Interfaces*, 2022, **14**, 9222–9230, DOI: 10.1021/acsami.1c24295.

34 P. Jacquet, B. Rémy, R. P. T. Bross, M. van Grol, F. Gaucher, E. Chabrière, M. C. de Koning and D. Daudé, Enzymatic decontamination of G-type, V-type and novichok nerve agents, *Int. J. Mol. Sci.*, 2021, **22**, 8152, DOI: 10.3390/ijms22158152.

35 M. Otsuka and H. Miyaguchi, Theoretical evaluation of the hydrolysis of conventional nerve agents and novichok agents, *Chem. Phys. Lett.*, 2021, **785**, 139116, DOI: 10.1016/j.cplett.2021.139116.

36 Y. A. Imrit, H. Bhakhoa, T. Sergeieva, S. Danés, N. Savoo, M. I. Elzagheid, L. Rhyman, D. M. Andrada and P. Ramasami, A theoretical study of the hydrolysis mechanism of A-234; the suspected novichok agent in the Skripal attack, *RSC Adv.*, 2020, **10**, 27884–27893, DOI: 10.1039/d0ra05086e.

37 R. Shi, L. Zhang, D. Ma and Z. Cao, Elucidating the degradation mechanism of the nerve agent A-234 using various detergents: A theoretical investigation, *Phys. Chem. Chem. Phys.*, 2024, **26**, 15292–15300, DOI: 10.1039/d4cp00881b.

38 S. L. Bartelt-Hunt, D. R. U. Knappe and M. A. Barlaz, A review of chemical warfare agent simulants for the study of environmental behavior, *Crit. Rev. Environ. Sci. Technol.*, 2008, **38**, 112–136, DOI: 10.1080/10643380701643650.

39 A. M. Ploskonka and J. B. DeCoste, Insight into organophosphate chemical warfare agent simulant hydrolysis in metal–organic frameworks, *J. Hazard. Mater.*, 2019, **375**, 191–197, DOI: 10.1016/j.jhazmat.2019.04.044.

40 J. Lavoie, S. Srinivasan and R. Nagarajan, Using cheminformatics to find simulants for chemical warfare agents, *J. Hazard. Mater.*, 2011, **194**, 85–91, DOI: 10.1016/j.jhazmat.2011.07.077.

41 T. Carvalho-Silva, L. Modesto-Costa, C. V. N. Borges, S. F. A. Cavalcante, R. B. Sousa, A. L. S. Lima and I. Borges, Synthesis, experimental and molecular dynamics simulation of the ESI-CID spectrum of the nerve agent Novichok analog O-2-methoxyethyl N-[bis(dimethylamino) methylidene]-P-methylphosphonamidate, *Int. J. Mass Spectrom.*, 2023, **490**, 117087, DOI: 10.1016/j.ijms.2023.117087.

42 M. C. Santos, F. D. Botelho, A. S. Gonçalves, D. A. S. Kitagawa, C. V. N. Borges, T. Carvalho-Silva, L. B. Bernardo, C. N. Ferreira, R. B. Rodrigues, D. C. F. Ferreira Neto, E. Nepovimova, K. Kuča, S. R. LaPlante, A. L. S. Lima, T. C. C. França and S. F. A. Cavalcante, Are the current commercially available oximes capable of reactivating acetylcholinesterase inhibited by the nerve agents of the A-series?, *Arch. Toxicol.*, 2022, **96**, 2559–2572, DOI: 10.1007/s00204-022-03316-z.

43 L. B. Bernardo, C. V. N. Borges, P. A. G. Buitrago, K. Kuča, S. F. A. Cavalcante, R. B. Sousa, A. L. S. Lima and D. A. S. Kitagawa, Synthesis and in vitro assessment of the reactivation profile of clinically available oximes on the acetylcholinesterase model inhibited by A-230 nerve agent surrogate, *Arch. Toxicol.*, 2024, **98**, 3397–3407, DOI: 10.1007/s00204-024-03821-3.

44 D. A. S. Kitagawa, M. C. Dos Santos, K. Kuča, T. C. C. França and S. F. d. A. Cavalcante, In vitro comparison of the acetylcholinesterase inhibition caused by V- and A-series nerve agents' surrogates, *Chem. Biol. Interact.*, 2023, **383**, 110678, DOI: 10.1016/j.cbi.2023.110678.

45 L. B. Bernardo, L. A. Vieira, C. V. N. Borges, P. A. G. Buitrago, K. Kuča, T. C. C. França, S. F. A. Cavalcante, R. B. Sousa, A. L. S. Lima and D. A. S. Kitagawa, In silico studies and in vitro evaluation of isatin-pyridine oxime hybrids as novel reactivators of acetylcholinesterase inhibited by an A-230 surrogate, *Arch. Toxicol.*, 2025, **99**, 2225–2228, DOI: 10.1007/s00204-025-03976-7.

46 F. Neese, Software update: The ORCA program system – Version 6.0, *WIREs Comput. Mol. Sci.*, 2025, **15**, e70019, DOI: 10.1002/wcms.70019.

47 B. de Souza, GOAT: A global optimization algorithm for molecules and atomic clusters, *Angew Chem. Int. Ed. Engl.*, 2025, **64**, e202500393, DOI: 10.1002/anie.202500393.

48 C. Bannwarth, S. Ehlert and S. Grimme, GFN2-xTB–An accurate and broadly parametrized self-consistent tight-binding quantum chemical method with multipole electrostatics and density-dependent dispersion contributions, *J. Chem. Theor. Comput.*, 2019, **15**, 1652–1671, DOI: 10.1021/acs.jctc.8b01176.

49 P. J. Stephens, F. J. Devlin, C. F. Chabalowski and M. J. Frisch, Ab initio calculation of vibrational absorption and circular dichroism spectra using density functional force fields, *J. Phys. Chem.*, 1994, **98**, 11623–11627, DOI: 10.1021/j100096a001.

50 S. Grimme, S. Ehrlich and L. Goerigk, Effect of the damping function in dispersion corrected density functional theory, *J. Comb. Chem.*, 2011, **32**, 1456–1465, DOI: 10.1002/jcc.21759.

51 F. Weigend and R. Ahlrichs, Balanced basis sets of split valence, triple zeta valence and quadruple zeta valence quality for H to Rn: Design and assessment of accuracy, *Phys. Chem. Chem. Phys.*, 2005, **7**, 3297–3305, DOI: 10.1039/b508541a.

52 C. J. C. Aleksandr, V. Mhd and M. Marenich, Universal solvation model based on solute electron density and on a continuum model of the solvent defined by the bulk dielectric constant and atomic surface tensions, *J. Phys. Chem. B*, 2009, **113**, 6378–6396, DOI: 10.1021/jp810292n.

53 N. Mardirossian and M. Head-Gordon, ωB97M-V: A combinatorially optimized, range-separated hybrid, meta-GGA density functional with VV10 nonlocal correlation, *J. Chem. Phys.*, 2016, **144**, 214110, DOI: 10.1063/1.4952647.

54 J. Zheng, X. Xu and D. G. Truhlar, Minimally augmented Karlsruhe basis sets, *Theor. Chem. Acc.*, 2011, **128**, 295–305, DOI: 10.1007/s00214-010-0846-z.

55 C. Riplinger, B. Sandhoefer, A. Hansen and F. Neese, Natural triple excitations in local coupled cluster calculations with pair natural orbitals, *J. Chem. Phys.*, 2013, **139**, 134101, DOI: 10.1063/1.4821834.

56 B. Helmich-Paris, B. de Souza, F. Neese and R. Izsák, An improved chain of spheres for exchange algorithm, *J. Chem. Phys.*, 2021, **155**, 104109, DOI: 10.1063/5.0058766.

57 S. Das, S. Chakraborty and R. Ramakrishnan, Critical benchmarking of popular composite thermochemistry models and density functional approximations on a probabilistically pruned benchmark dataset of formation enthalpies, *J. Chem. Phys.*, 2021, **154**, 044113, DOI: 10.1063/5.0032713.

58 S. Das, S. Senthil, S. Chakraborty and R. Ramakrishnan, All Hands on Deck: Accelerating Ab Initio Thermochemistry via Wavefunction Approximations, *ChemRxiv*, Preprint, chemrxiv:14524890.v1, 2021, DOI: 10.26434/chemrxiv.14524890.v1.

59 T. Lu and F. Chen, Multiwfn: A multifunctional wavefunction analyzer, *J. Comb. Chem.*, 2012, **33**, 580–592, DOI: 10.1002/jcc.22885.

60 T. Lu, A comprehensive electron wavefunction analysis toolbox for chemists, Multiwfn, *J. Chem. Phys.*, 2024, **161**, 082503, DOI: 10.1063/5.0216272.

61 W. Humphrey, A. Dalke and K. Schulten, VMD: Visual Molecular Dynamics, *J. Mol. Graph.*, 1996, **14**, 33–38, DOI: 10.1016/0263-7855(96)00018-5.

62 A. V. Marenich, W. Ding, C. J. Cramer and D. G. Truhlar, Resolution of a challenge for solvation modeling: Calculation of dicarboxylic acid dissociation constants using mixed discrete–continuum solvation models, *J. Phys. Chem. Lett.*, 2012, **3**, 1437–1442, DOI: 10.1021/jz300416r.

63 T. Xu, J. Chen, X. Chen, H. Xie, Z. Wang, D. Xia, W. Tang and H.-B. Xie, Prediction models on pK_a and base-catalyzed hydrolysis kinetics of parabens: Experimental and

quantum chemical studies, *Environ. Sci. Technol.*, 2021, **55**, 6022–6031, DOI: 10.1021/acs.est.0c06891.

64 J. Blotevogel, A. N. Mayeno, T. C. Sale and T. Borch, Prediction of contaminant persistence in aqueous phase: A quantum chemical approach, *Environ. Sci. Technol.*, 2011, **45**, 2236–2242, DOI: 10.1021/es1028662.

65 T. Lu, TSTcalculator, http://sobereva.com/310, accessed on 28 May, 2025.

66 C. Doubleday, R. Armas, D. Walker, C. V. Cosgriff and E. M. Greer, Heavy-atom tunneling calculations in thirteen organic reactions: Tunneling contributions are substantial, and Bell's formula closely approximates multidimensional tunneling at ≥250 K, *Angew Chem. Int. Ed. Engl.*, 2017, **56**, 13099–13102, DOI: 10.1002/anie.201708489.

67 F. Cramer and A. Vollmar, Zur Chemie der "energiereichen phosphate", II. Acylierung von Guanidinen und Amidinen mit Chloriden und Anhydriden der Phosphorsaure, *Chem. Ber.*, 1958, **91**, 911–918, DOI: 10.1002/cber.19580910504.

68 B. Picard, I. Chataigner, J. Maddaluno and J. Legros, Introduction to chemical warfare agents, relevant simulants and modern neutralisation methods, *Org. Biomol. Chem.*, 2019, **17**, 6528–6537, DOI: 10.1039/c9ob00802k.

69 S. Webb, F. Coulon and T. Temple, A critical review of liquid, low toxicity chemical warfare agent simulants: Enhancing accuracy, safety, and methodological approaches for sampling, *J. Hazard. Mater.*, 2025, **492**, 138021, DOI: 10.1016/j.jhazmat.2025.138021.

70 T. Lu, On the judgement whether a reaction is easy to occur based on potential barrier, http://sobereva.com/506, accessed 28 May, 2025.

71 S. J. Admiraal and D. Herschlag, The Substrate-Assisted General Base Catalysis Model for Phosphate Monoester Hydrolysis: Evaluation Using Reactivity Comparisons, *J. Am. Chem. Soc.*, 2000, **122**, 2145–2148, DOI: 10.1021/ja993942g.

72 F. Duarte, J. Åqvist, N. H. Williams and S. C. L. Kamerlin, Resolving apparent conflicts between theoretical and experimental models of phosphate monoester hydrolysis, *J. Am. Chem. Soc.*, 2015, **137**, 1081–1093, DOI: 10.1021/ja5082712.